ACS ORGANIC & INORGANIC Au
AN OPEN ACCESS JOURNAL OF THE AMERICAN CHEMICAL SOCIETY

pubs.acs.org/orginorgau
Article

Zinc(II) Complexes of SIRTi1/2 Analogues Transmetallating with Copper Ions and Inducing ROS Mediated Paraptosis

Published as part of ACS Organic & Inorganic Au virtual special issue "2023 Rising Stars in Organic and Inorganic Chemistry".

Ashwini Kumar, Ayushi Chaudhary, Himanshu Sonker, Seemadri Subhadarshini, Mohit K. Jolly, and Ritika Gautam Singh*

Cite This: ACS Org. Inorg. Au 2024, 4, 319−328

Read Online

ACCESS | Metrics & More | Article Recommendations | Supporting Information

ABSTRACT: As the SIRT*i* analogue series (HL1−HL6) show potent antitumor activity in vitro, we synthesized their corresponding zinc(II) complexes (ZnL1−ZnL6) and investigated their potential as anticancer agents. The Zn(II) complexes showed substantially greater cytotoxicity than HL1−HL6 alone in several cancer cell-types. Notably, distinct structure−activity relationships confirmed the significance of *tert*-butyl (ZnL2) pharmacophore inclusion in their activity. ZnL2 complexes were found to transmetalate with copper ions inside cells, causing the formation of redox-active copper complexes that induced reactive oxygen species (ROS) production, mitochondrial membrane depolarization, ATP decay, and cell death. This is the first study to exhibit Zn(II) complexes that mediate their activity via transmetalation with copper ions to undergo paraptosis cell death pathway. To further confirm if the SIRT1/2 inhibitory property of SIRTi analogues is conserved, a docking simulation study is performed. The binding affinity and specific interactions of the Cu(II) complex obtained after transmetalation with ZnL2 were found to be higher for SIRT2 (K_i = 0.06 μM) compared to SIRT1 (K_i = 0.25 μM). Thus, the concurrent regulation of several biological targets using a single drug has been shown to have synergistic therapeutic effects, which are crucial for the effective treatment of cancer.

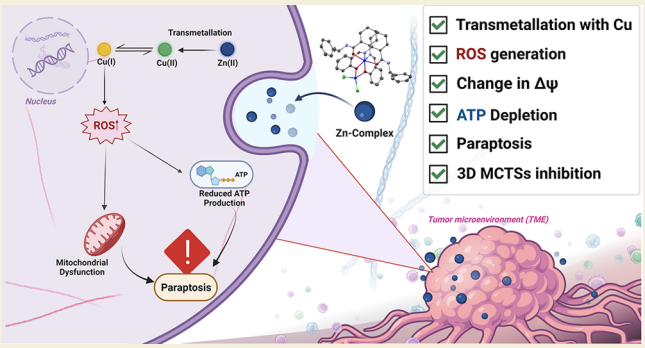

KEYWORDS: *Anticancer, SIRTi1/2, Paraptosis, Transmetalation, Reactive Oxygen Species, 3D Multicellular Tumour Spheroids*

INTRODUCTION

Sirtinol, also known as ALX-270-308, is a pharmacological compound that exhibits preferential inhibition toward NAD^+-dependent deacetylases SIRT1 and SIRT2 due to its structural similarity with other on par comparable sirtuin inhibitors, especially cambinol and splitomicin, which possess the β-naphthol pharmacophore.[1] Since their identification as a potential anticancer agent, sirtinol and their corresponding transition metal complexes (Fe(II), Fe(III), Cu(II), and Zn(II)) have become the subject of significant research and development.[2] The anticancer effectiveness of sirtinol was initially attributed to its capacity to impede the activation of the Ras-MAPK pathway.[3] Subsequent investigations revealed that the observed effect constituted merely a portion of their overall activity, as the production of redox-active metal complexes leading to the generation of reactive oxygen species (ROS) played a significant role in their mode of action.[4]

Sirtinol employs the O−N−O coordination group, and previous studies have indicated that inhibitors employing the O−N−O donor structure in the formation of complexes with transition metals exhibit enhanced cytotoxicity against various cancer cell lines.[5] Other N−N−S donor system complexes, such as 3-AP, have also exhibited improved cytotoxicity. Notably, 3-AP has been involved in more than 20 multicenter clinical trials. Nevertheless, 3-AP has encountered other challenges, such as limited effectiveness in certain types of tumors and the occurrence of severe adverse reactions, notably methemoglobinemia.[6]

Sirtinol, classified as a first-generation SIRT1/2 HDACi, is now in the preclinical stages of research. However, in comparison to other inhibitors, they have undergone little therapeutic development, leaving ample room for further exploration and investigation. This led to the conception and

Received: September 29, 2023
Revised: February 1, 2024
Accepted: February 1, 2024
Published: February 26, 2024

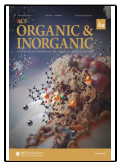

Scheme 1. Synthesis of ZnL1−ZnL6 Complexes

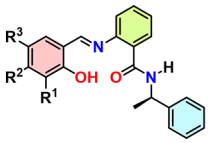

$ZnCl_2$
TEA, MeOH, RT
$[Zn_2Lx_2Cl_2]$
x = 1 to 6

Compounds				Compounds			
ZnL1	R^1 = H	R^2 = H	R^3 = H	ZnL4	R^1 = H	R^2 = H	R^3 = Br
ZnL2	R^1 = ^{t}Bu	R^2 = H	R^3 = ^{t}Bu	ZnL5	R^1 = H	R^2 = H	R^3 = F
ZnL3	R^1 = H	R^2 = H	R^3 = Cl	ZnL6	R^1 = H	R^2 = H	R^3 = NO_2

creation of the second-generation counterparts of sirtinol as well as their transition metal complexes. Additionally, we explored the potential of these compounds to retain their inhibitory effects on SIRT1/2. In our previous study, through extensive structure−activity relationship, *de novo* (*R*,*E*)-2-((2-hydroxybenzylidene)amino)-*N*-(1-phenylethyl)benzamide series was designed by including 2-hydroxy benzaldehyde moiety into the structural backbone derived from sirtinol.[7] The study demonstrated that the benzaldehyde analogues of sirtinol (HL1−HL6) and their corresponding Cu(II) complexes $Cu(L1)_2$−$Cu(L6)_2$ find application as an efficient candidate for chemodynamic therapy (CDT). The Cu(II) complexes has potential to disrupt redox homeostasis and participate in reactive oxygen species mediated glutathione (GSH) depletion, mitochondrial membrane depolarization, lipid peroxidation (LPO), DNA damage, and ultimately, activates Unfolded Protein Response (UPR) cascade by endoplasmic reticulum stress which leads to an anticancer property.

Herein, we utilized the second generation (*R*,*E*)-2-((2-hydroxybenzylidene)amino)-*N*-(1-phenylethyl)benzamide series ligands to synthesize their dimeric ZnL1−ZnL6 complexes. The antiproliferative effects of ZnL1−ZnL6 complexes were studied in various cancer cell types, and importantly, the Zn(II) complexes demonstrated substantially greater cytotoxicity than their corresponding ligands itself. Significantly, we demonstrate that ZnL2, ZnL3, and ZnL4 exchange metal centers with copper ions to produce redox-active copper complexes that facilitate ROS production and cytotoxicity. The mechanistic evaluation demonstrates that predominantly the complex follows paraptosis, a programmed cell death pathway. Taking into consideration the translational aspect of this proposed drug candidate and to avoid failure arising while transitioning from 2D monolayer cell cultures to in vivo models, the efficacy of ZnL2 is also investigated on 3D multicellular tumor spheroids (MCTSs).

RESULTS AND DISCUSSION

Synthesis and Characterization of *De Novo* ZnL1−ZnL6 Complexes

Ligands HL1−HL6 were synthesized according to previously reported method.[7] A series of Zn(II) complexes were prepared from HL1−HL6 ligands at 1:1 (Scheme 1) [Zinc(II)/ligand] molar ratios. The empirical 1:1 Zn(II) complexes were synthesized via the reaction of equimolar amounts of the ligands and anhydrous $ZnCl_2$ in methanol in the presence of triethylamine. All complexes were characterized by ^1H and ^{13}C NMR, IR, UV−vis, and ESI-MS, and their purity was assessed by HPLC and determined to be >95%. As anticipated, HL1−HL6 formed neutral dimeric 1:1 (Zinc(II)/ligand) complexes with $ZnCl_2$ upon deprotonation of the benzylic phenol scaffold in the presence of the base triethylamine (Scheme 1).

Single-Crystal X-ray Analysis

Out of six ZnL1−ZnL6 complexes, four of the Zn(II) complexes, namely, ZnL1, ZnL3, ZnL4, and ZnL6, were subjected to structural characterization by using single crystal X-ray analysis. The insight into the molecular structure of these compounds facilitates better understanding of their biological activity. The ORTEP diagrams of the Zn(II) complexes ZnL1, ZnL3, ZnL4, and ZnL6 along with the partial labeling scheme are depicted in Figure 1. The crystal data and structural refinement parameters are summarized in Tables S1−S4.

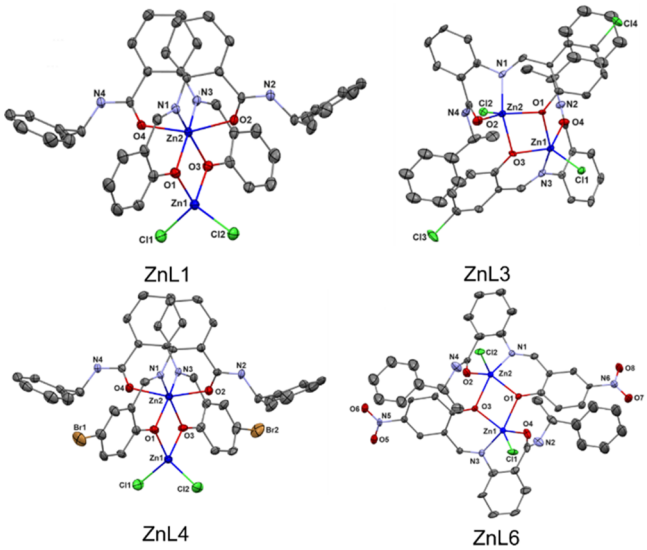

Figure 1. Crystal structure of ZnL1 (CCDC 2294884), ZnL3 (CCDC 2294883), ZnL4 (CCDC 2294885), and ZnL6 (CCDC 2295142) showing a partial labeling scheme. Thermal ellipsoids are scaled to the 50% probability level.

The analysis of the X-ray data for the single crystal indicated that the complexes are dinuclear. Despite having the same empirical formula, the molecular structures can be grouped into two categories. In the first case, ZnL1 and ZnL4 exhibit two different geometric zinc center (Zn1: distorted tetrahedral and Zn2: distorted octahedral) configurations, whereas ZnL3 and ZnL6 display a comparable (Zn1 and Zn2 pentacoordinate) geometric arrangement. In ZnL1 and ZnL4, X-ray results revealed that the ZnL1 complex crystallizes in a tetragonal unit cell in the space group $P4_32_12$ while the ZnL4 complex crystallizes in an orthorhombic unit cell in the space group $P2_12_12_1$. The Zn2 center in the six-coordinate complex is present in a distorted octahedral environment. It forms bonds with two imine nitrogen atoms, N1 and N3, as well as two phenoxide anions, O1 and O3. The two remaining coordination sites are occupied by oxygen atoms, specifically,

https://doi.org/10.1021/acsorginorgau.3c00052
ACS Org. Inorg. Au 2024, 4, 319−328

Table 1. λ_{max} Absorption and Emission peaks for HL1−HL6 and ZnL1−ZnL6

compound	λ_{max} (absorption, nm)	compound	λ_{max} (absorption, nm)	λ (excitation, nm)	λ (emission, nm)
HL1	268, 338	ZnL1	286, 397	395	502
HL2	279, 354	ZnL2	302, 422	420	547
HL3	350	ZnL3	288, 409	408	513
HL4	270, 350	ZnL4	288, 408	408	512
HL5	266, 348	ZnL5	286, 410	408	511
HL6	331, 400	ZnL6	280, 347	345	417

Table 2. Cytotoxicity Values of ZnL1−ZnL6 on Cell Lines, Assessed by Resazurin Assay

	Cell growth inhibition, IC_{50} (μM), 72 h			
compounds	MCF-7	A549	MDA-MB-231	PC3
ZnL1	41.66 ± 5.80	52.13 ± 29.64	35.50 ± 2.30	32.34 ± 3.76
ZnL2	8.41 ± 2.40	29.76 ± 2.31	13.41 ± 3.52	13.00 ± 3.00
ZnL3	29.07 ± 6.00	38.97 ± 1.64	31.63 ± 1.85	36.16 ± 0.42
ZnL4	31.07 ± 5.91	37.75 ± 1.53	28.66 ± 2.76	31.41 ± 1.39
ZnL5	32.70 ± 2.48	32.86 ± 2.30	55.28 ± 2.61	62.81 ± 5.10
ZnL6	67.47 ± 3.80	>100	>100	>100
cisplatin	6.39 ± 1.57	4.13 ± 0.14	1.9 ± 0.10	3.14 ± 0.22

O2 and O4, which are part of the carbonyl moiety. The coordination geometry of Zn1 is characterized as a distorted tetrahedral geometry, resulting from the bonding of two phenoxide anions (O1 and O3) and two chloride anions (Cl1 and Cl2). Hence, it can be shown that both phenoxide anions O1 and O3 serve as a connecting link between the Zn1 and Zn2 atoms, as depicted in Figure 1 and detailed in Tables S2−S4. The typical bond lengths (Å) for Zn−O (phenoxo, Ar−O^-), Zn−O (carbonyl, C═O), and Zn−N (imine, C═N) are detailed in Tables S1−S3.

However, ZnL3 and ZnL6 formed pentacoordinated dinuclear complexes of distorted square pyramidal geometry. Here, the ZnL3 complex crystallizes in a trigonal unit cell in space group $P3_2$, whereas the ZnL6 complex crystallizes in a triclinic unit cell in space group $P1$. In both of these complexes, the five coordinated Zn1 and Zn2 centers bonded to one imine nitrogen N1 and N3, respectively, two phenoxide anions, O1 and O3 in the basal equatorial plane, and the other coordination site is bonded to oxygen atoms O2 and O4 of the carbonyl moiety. The axial location is covalently connected to chlorine atoms Cl1 and Cl2, respectively (Figure 1, Tables S1−S3). The bond lengths and bond angles (Å) are detailed in Tables S1−S3.

Collectively, these physical analyses provide evidence that two coordination forms of dinuclear 2:2 Zn(II) complexes can form. While the chemical nature of zinc complexes in solid form is well understood, their actual chemical species in solution remain unknown, but they are biologically significant and should be considered when evaluating their activity.

UV−Visible and Fluorescence Spectroscopic Assessment of the ZnL1−ZnL6 Complexes

The HL1−HL6, exhibit an intense peak in the UV region with a λ_{max} at 350−365 nm in MeOH (Figure S13). These are assigned to $n \rightarrow \pi^*$ and/or $\pi \rightarrow \pi^*$ transitions. Nevertheless, the introduction of Zn(II) resulted in the emergence of a distinct peak within the visible spectrum, with a maximum wavelength (λ_{max}) falling within the range of 400−420 nm (see Table 1 for λ_{max}), which is a hallmark of ligand−metal charge transfer transitions from Zn(II) to phenoxide (Figure S13). The stability of the Zn(II) complexes is also analyzed by UV−vis absorption spectroscopy. As shown in Figure S15, the time-dependent UV−vis spectra of ZnL1−ZnL6 in organic solution methanol displayed no hypsochromic and bathochromic shifts at 0, 24, and 48 h, indicating that ZnL1−ZnL6 were stable in solution at room temperature for 48 h. The stability study was restricted to organic solvents, as compounds undergo a certain degree of hydrolysis in aqueous buffer conditions. This characteristic represents a possible advantage of metal-based anticancer therapies in comparison to organic compounds.[8]

Fluorescence spectra of complexes ZnL1−ZnL6 (Figure S14) were also measured in MeOH following excitation between 345 and 420 nm (Table 1). All Zn(II) complexes fluoresced in the green region of the visible spectrum, which opens up possibilities for fluorescence-based cellular imaging.

Cytotoxicity of Zn(II) Complexes (ZnL1−ZnL6), as Evaluated by Resazurin Assay in Different Tumor Cell Types

The anticancer activities of the complexes ZnL1−ZnL6 were evaluated by means of a resazurin-based viability assay in breast adenocarcinoma cell lines MDA-MB-231 and MCF-7, human lung adenocarcinoma cell line A549, and human prostate cancer cell line PC3 in the presence of FDA approved cisplatin as the positive control (Tables 2 and Figures S17−S20). The IC_{50} values (Table 2), extrapolated from the dose−response curves reported in Figures S17−S20, allowed us to identify the following structure−activity relationships: (i) Most dinuclear zinc complexes showed considerable cytotoxicity toward breast adenocarcinoma cell line MCF-7 as compared to other cells, demonstrating selective cytotoxicity, (ii) ZnL2 with *tert*-butyl atoms at the R1 and R3 positions displayed higher or comparable antiproliferative activity in MCF-7 (IC_{50} = 8.41 ± 2.40 μM) cells to cisplatin in MCF-7 (IC_{50} = 6.39 ± 1.57 μM). Thus, the strongly electron-donating lipophilic substituent *tert*-butyl of 2-hydroxybenzaldehyde at R1 and R3 position increased the antitumor activity across all cancer cell lines that are investigated here. Further mechanistic experiments were conducted on the ZnL2 complex, which exhibited the highest activity.

https://doi.org/10.1021/acsorginorgau.3c00052
ACS Org. Inorg. Au 2024, 4, 319−328

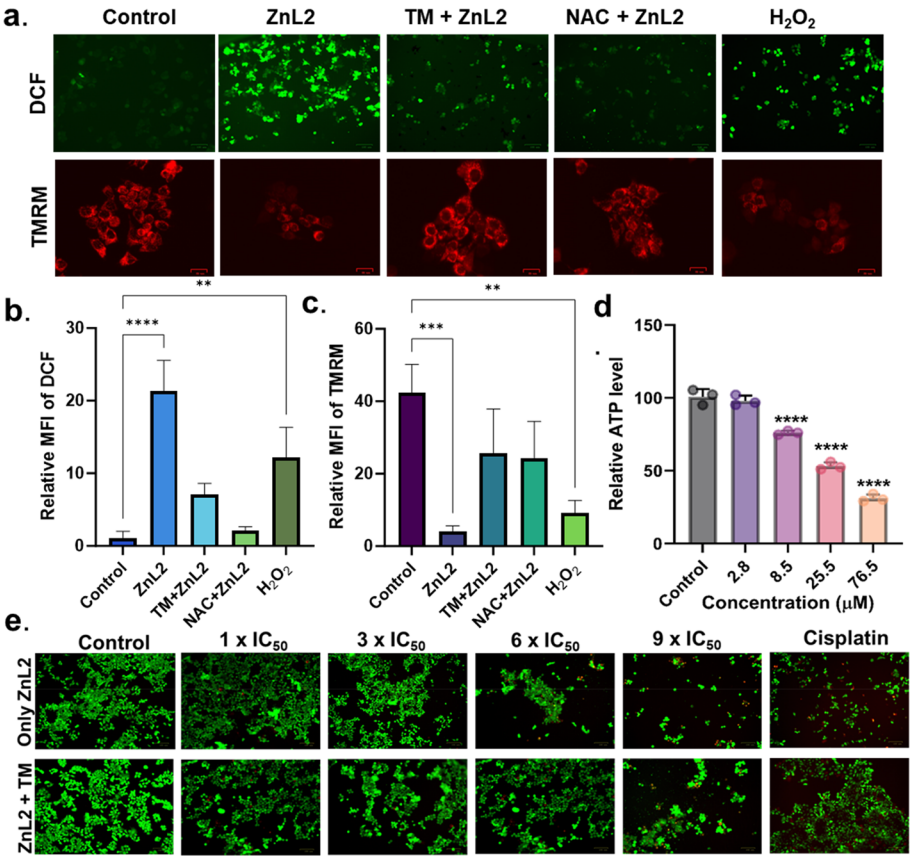

Figure 2. (a) (Top) ROS generation by ZnL2 in MCF-7 cancer cells with the H_2DCF-DA dye after 4 h incubation. Scale bar = 100 μm. All images were captured with a BIO-RAD ZOE fluorescent cell imager. (Bottom) Change in Mitochondrial membrane potential ($\Delta\Psi_m$) observed by TMRM dye staining on MCF-7 cell lines with different concentrations of ZnL2 after 3 h of incubation. Scale bar = 25 μm. (b) Bar graph of mean fluorescence intensity (MFI) of DCF assay calculated using ImageJ software. (c) Bar graph of mean fluorescence intensity (MFI) of TMRM assay calculated using ImageJ software. (d) Cellular ATP production by CellTiter-Glo luminescence assay in the presence of ZnL2. (e) Live/Dead assay performed on MCF-7 cell line in the presence of ZnL2 and TM treated ZnL2 after 24 h of incubation. [Calcein-AM] = 2.0 μM whereas [Propidium Iodide] = 4.5 μM were treated for 15 min. Scale bar = 100 μm. Images were collected using a BioRad fluorescent cell imager. *$p < 0.05$, **$p < 0.01$, ***$p < 0.001$, ****$p < 0.0001$. $n = 3$.

ZnL2−ZnL4 Undergoing Transmetalation with Copper Ions

The titration by UV−visible spectroscopic method confirms that, in agreement with the Irving−Williams series, HL1−HL6 have an overall higher binding affinity for Cu(II) over Zn(II). Herein, to investigate the potential to undergo transmetalation, increasing concentrations of $Cu(OAc)_2$ were added to the Zn(II) complexes and the absorption spectra was recorded using a UV−vis spectrophotometer. The addition of increasing concentrations of Cu(II) salt resulted in the shift in absorbance spectra away from ZnL2, ZnL3, ZnL4 toward their respective Cu(II) complexes (Figure S16). The UV−vis spectra also displayed well-defined isosbestic points (ZnL2 = 339, 393 nm; ZnL3 = 331, 422 nm; ZnL4 = 331, 421 nm), this further demonstrated that transmetalation proceeded cleanly on addition of Cu(II) salt. This transmetalation is consistent with the previous reported studies which displayed the complete replacement of Zn(II) complexes in the presence of Cu(II) ion.[9]

In-Cell Transmetalation Assay

Given that the dinuclear zinc complex (Zn(II)/ligand) does not display redox activity, but the zinc complexes demonstrate increased cytotoxicity (Table 2) compared to the ligands alone, our subsequent inquiry aimed to explore the possibility that the cytotoxicity of the zinc complexes could be attributed to transmetalation, encompassing the substitution of Zn(II) with Cu(II). The evaluation of the agents' capacity to facilitate the production of reactive oxygen species (ROS) was conducted in these investigations by assessing the oxidation of the nonfluorescent, redox-active probe, 2′,7′-dichlorodihydrofluorescein (H_2DCF), into the intensely fluorescent end-product, 2′,7′-dichlorofluorescein (DCF). It is worth mentioning that DCF (2′,7′-dichlorofluorescin) is a widely recognized redox probe that is frequently employed for the quantification of reactive oxygen species (ROS) production.

The oxidation of H_2DCF to DCF was evaluated inside the MCF-7 cancer cell system (Figure 2a). As expected, ZnL2 alone did not lead to an increase in DCF fluorescence. However, in accordance with previous studies in our lab, $Cu(L2)_2$ is exceedingly redox active, resulting in a significant increase in DCF fluorescence relative to that of ZnL2 (Figure 2a). This redox activity was abolished by the supplement of the nontoxic copper chelator ammonium tetra-thiomolybdate (TM), to ZnL2 + Cu(II), which caused a substantial decline in DCF fluorescence. These data suggest that although ZnL2 itself was not redox active, in the existence of copper ions, transmetalation occurs, leads to formation of a redox active Cu(II) complex that can mediate the oxidation of H_2DCF to DCF.[10]

https://doi.org/10.1021/acsorginorgau.3c00052
ACS Org. Inorg. Au 2024, 4, 319−328

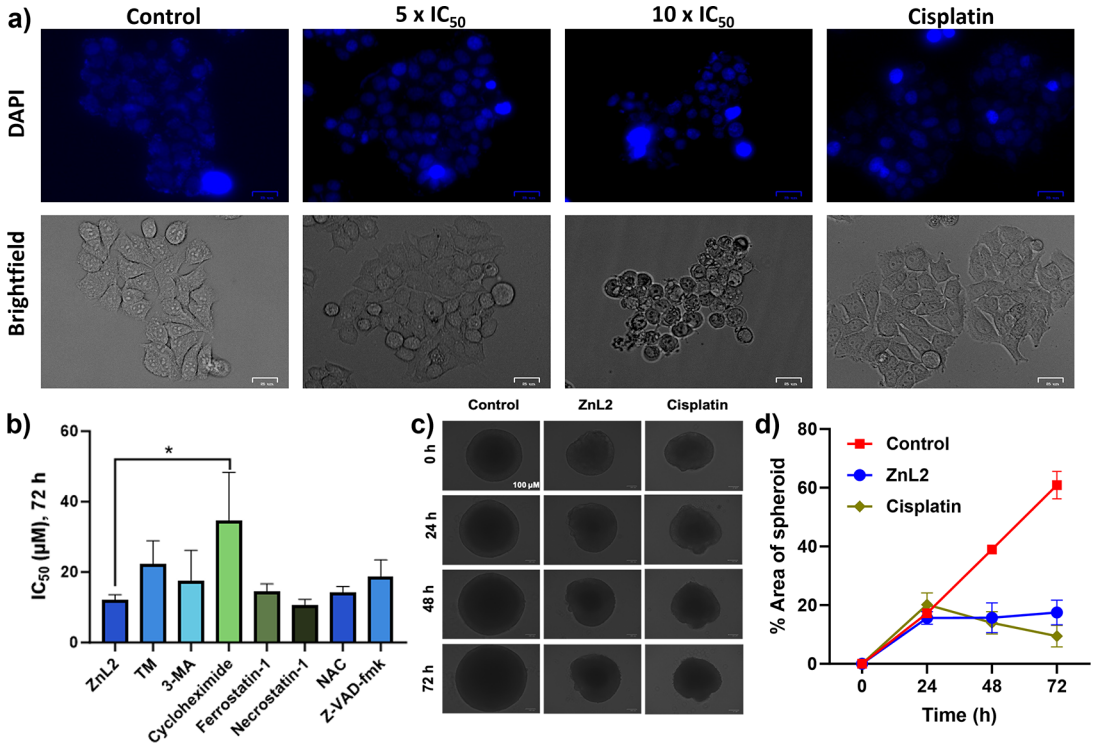

Figure 3. (a) Cellular and nuclear morphology of cancer cells after DAPI staining. MCF-7 cells were treated with ZnL2 for 3 h and stained with DAPI. Cisplatin and DMSO were taken as positive and negative control, respectively. Images were collected using BioRad fluorescent cell imager. Scale = 25 μm. (b). IC_{50} values of ZnL2 against MCF-7 cells in the presence of inhibitors. TM and inhibitors were preincubated for 1 h, and the ZnL2 was then loaded and incubated for 72 h in normoxic conditions. (c). Bright-field images of MCF-7 MCTSs treated with IC_{50} concentration of ZnL2 observed at 0, 24, and 48 h. Untreated MCTSs were taken as control, whereas cisplatin (10 μM) treated was taken as positive control. Scale bar = 100 μm. (d) Percentage area increase of spheroid calculated by ImageJ software. *$p < 0.05$, **$p < 0.01$, and ***$p < 0.001$. $n = 3$.

Mitochondrial Membrane Potential Change and Decay in ATP Production Mediated by ZnL2

Free radicals, such as hydroxyl radicals ($^{\bullet}OH$) and other oxygen-centered species, have been demonstrated to interfere with several cellular macromolecules including those comprising the electron transport chain. Consequently, this leads to the impairment of the mitochondrial energy cascade. It is increasingly recognized that mitochondrial dysfunction plays a pivotal role in driving cell death process.[11] We assessed the mitochondrial membrane potential ($\Delta\Psi_m$) as an indicator of metabolic activity, particularly in relation to oxidative phosphorylation facilitating ATP synthesis. This was accomplished by quantifying the accumulation of TMRM within the mitochondrial matrix, a measure that corresponds directly to the $\Delta\Psi_m$ levels. Notably, the TMRM signal is robust for mitochondria with high $\Delta\Psi_m$, indicative of polarization (i.e., healthy mitochondria), and weaker for depolarized or unhealthy mitochondria. The uptake of TMRM by mitochondria serves to distinguish between cells undergoing apoptosis and those in a healthy state.

The cells were exposed to TM and NAC for 2 h before the treatment of the ZnL2 complex. Here, H_2O_2 was taken as the positive control, whereas DMSO (0.3%) treated cells were taken as the negative control (Figure 2b). Following exposure to ZnL2, a discernible shift in the mitochondrial membrane potential was noted, signifying the depolarization of the mitochondrial membrane potential. However, TM and NAC pretreated cells were showing polarized membrane potential as the cells were showing bright fluorescence. A heightened Mean Fluorescence Intensity (MFI) denotes the vitality of control cells with intact $\Delta\Psi_m$. Conversely, treatment with only ZnL2 led to a significant decrease in MFI (10-fold) (Figure 2c). The MFI was calculated with the help of ImageJ software.

The experiment involving CellTiter-Glo was performed to evaluate its influence on cellular metabolic processes. The present test is designed to measure the quantities of adenosine triphosphate (ATP) within cells, therefore functioning as a reliable indicator of their metabolic activity.[12] Given the role of $\Delta\Psi_m$ in mitochondrial ATP synthesis, we investigated ATP levels within MCF-7 cancer cell lines following exposure to varying concentrations (2.8, 8.5, 25.5, and 76.5 μM) of ZnL2 for 12 h, using the bioluminescence-based CellTiter-Glo assay. Notably, ZnL2 induced a prompt and dose-dependent decline in the ATP content in MCF-7 cells, as evidenced in Figure 2d.

Collectively, the results obtained from both the TMRM and ATP production assays clearly indicate a disturbance in mitochondrial function following treatment with ZnL2. Notably, when cells were pretreated with the nontoxic copper chelator, TM, the impact of the zinc complex was significantly attenuated compared to its effect when administered alone. This strongly suggests that ZnL2 does not exhibit redox activity on its own. However, when copper ions are present, transmetalation takes place, leading to the formation of a redox active $Cu(L2)_2$ complex. This complex is capable of facilitating the oxidation of H_2DCF to DCF.

Apoptosis Live–Dead Cell Analysis

To elucidate the mechanisms of cytotoxicity in MCF-7 cells, the impact of ZnL2, in the presence and absence of ammonium tetrathiomolybdate (TM), was investigated. TM was pretreated 1 h before treatment with ZnL2. The evaluation of

https://doi.org/10.1021/acsorginorgau.3c00052
ACS Org. Inorg. Au 2024, 4, 319–328

cellular viability was undertaken through the utilization of Calcein-AM and Propidium Iodide staining, which, respectively, facilitated the discrimination between live and dead cells. As exemplified in Figure 2e, MCF-7 cells were treated with ZnL2. Following a 24 h incubation period involving various concentrations of ZnL2 ($1 \times IC_{50}$, $3 \times IC_{50}$, $6 \times IC_{50}$, and $9 \times IC_{50}$), a positive control (cisplatin), and a negative control (DMSO), the outcomes were assessed.

At the IC_{50} concentration, there was a notable increase in the green fluorescence stemming from Calcein-AM. However, beyond the IC_{50} threshold, there was an elevation in the intensity of red fluorescence, accompanied by a decrease in the cell population compared to that of the negative control (Figure 2e). These observations collectively imply the proficient capacity of ZnL2 to instigate apoptotic cell death within the MCF-7 cell line, aligning coherently with the overarching cytotoxicity analysis. Correspondingly, when considering the influence of TM, a similar pattern emerged, albeit with a higher cell population than in cases in which TM treatment was absent. This series of evidence confirms the intracellular transmetalation of the zinc complex.

DAPI Staining

The fluorescent dye known as DAPI (4′,6-diamidino-2-phenylindole) exhibits a high affinity for DNA regions that are rich in A−T base pairs. This dye is useful in facilitating the observation of chromatin condensation and nuclear damage. The differentiation between viable cells and apoptotic cells is achieved by the utilization of a staining technique that renders the distinctively condensed nuclei of the latter prominently blue in color. Hence, the staining methodology was employed to identify the occurrence of cellular apoptosis caused by ZnL2 in MCF-7 cells. Based on the findings (Figure 3a), it was determined that the nuclear structure of the untreated control cells remained intact. However, the MCF-7 cells treated with ZnL2 exhibited observable morphological alterations that are characteristic of apoptosis. These changes include cell shrinkage, membrane blebbing, increased staining intensity, chromatin condensation, fragmentation of nuclei, and the presence of apoptotic bodies. The cellular morphology of MCF-7 cells is observed to exhibit a round shape (Figure 3a through brightfield pictures).

Paraptosis Cell Death Mechanistic Pathways

To further understand the biological profile and the mechanistic pathway being followed by the Zn(II) complexes, we examined the impact of ZnL2 on cell death pathways within MCF-7 cells through the assessment of cytotoxicity in the presence of targeted inhibitors for specific cell death routes. These inhibitors included ammonium tetra thiomolybdate (TM, a nontoxic copper chelator), 3-methyladenine (autophagy), cycloheximide (paraptosis), ferrostatin-1 (ferroptosis), necrostatin-1 (necrosis), *N*-acetyl cysteine (NAC, a reactive oxygen species scavenger), and Z-VAD-fmk (apoptosis). Notably, a significant 3-fold increase in the IC_{50} value of the ZnL2 complex was observed in MCF-7 cells treated with the paraptosis inhibitor as shown in Figure 3b. Moreover, a 2-fold rise in IC_{50} was recorded in TM-treated cells, indicative of transmetalation events and the subsequent formation of an intracellular copper complex.[13−15] This confirms the paraptosis mediated cell death pathway being followed by the cells in the presence of our compound.

Spheroid Inhibition Assay

Having established the suitability of compounds in 2D monolayer cell culture settings, the efficacy of ZnL2 probe was investigated on 3D multicellular cancer spheroids (MCTSs). MCTSs have gained prominence as an in vitro model for gauging the therapeutic potential of drugs. This study's advantage lies in the fact that 2D cell cultures struggle to replicate 3D physiological conditions, leading to the failure of numerous anticancer agents to transition positively from 2D monolayer cells found in 96 well plates to in vivo mouse models. Tumours that exist within living organisms are distinguished by complex structures consisting of multiple layers, which provide intricate connections between cells. These interactions pose a significant challenge to the effective delivery of drugs. MCTSs, akin to their in vivo counterparts, exhibit analogous viable cellular interactions including tight junctions and extracellular matrix deposition. Moreover, they exhibit constraints on the diffusion of drugs. Moreover, akin to tumors in living organisms, multicellular tumor spheroids (MCTSs) exhibit the formation of a necrotic core in conjunction with hypoxic areas, hence playing a role in the development of drug resistance during cancer treatment. In aggregate, these characteristics make MCTSs a valuable in vitro model for a more accurate assessment of medication efficacy compared with 2D monolayer cells.

Consequently, we generated MCTSs using MCF-7 cells with an approximate diameter of 400−500 μm to assess the cytotoxic impact of ZnL2. Figure 3c and d illustrates the ZnL2-induced inhibition in MCTS growth. After 72 h, control MCTSs exhibited a 62% growth rate, whereas those treated with ZnL2 displayed an approximately 17% growth rate analyzed by ImageJ software. Nevertheless, when we conducted a morphological assessment of the MCTSs, it became evident that the boundaries of the MCTSs exhibited signs of structural disruption over time. This observation suggests that the drug treatment indeed had a discernible impact on the MCTSs.

Cellular Uptake

The overall efficacy of metal-based anticancer drugs is influenced by their internalization into cellular structures. In our study, we observed that the cytotoxic effects of a zinc complex were more pronounced in MCF-7 cells compared with other cell types. Consequently, MCF-7 cells were selected as the subject of investigation for the intracellular uptake of this zinc complex (referred to as ZnL2) and zinc chloride ($ZnCl_2$) using inductively coupled plasma mass spectrometry (ICP-MS). Following an 8 h treatment of MCF-7 cells with ZnL2, a significant increase in intracellular zinc content was observed in comparison to both the control group and cells treated with the metal salt $ZnCl_2$. The order of cellular uptake was as follows: ZnL2 > $ZnCl_2$ > control (Figure S22). These findings clearly demonstrate that the overall cellular uptake of the zinc complex, characterized by *tert*-butyl groups at positions R1 and R3 of salicylaldehyde, is notably higher than that of $ZnCl_2$. Moreover, the results from cytotoxicity assays and cellular uptake measurements suggest a correlation between the antiproliferative activity of ZnL2 and its cellular uptake efficiency.

SIRT1 and SIRT2 Inhibition Study

Our mechanistic study illustrates the role of intracellular copper ions on the cytotoxicity of the Zn(II) complexes. While the zinc complexes are not redox active, availability of Cu(II)

https://doi.org/10.1021/acsorginorgau.3c00052
ACS Org. Inorg. Au 2024, 4, 319−328

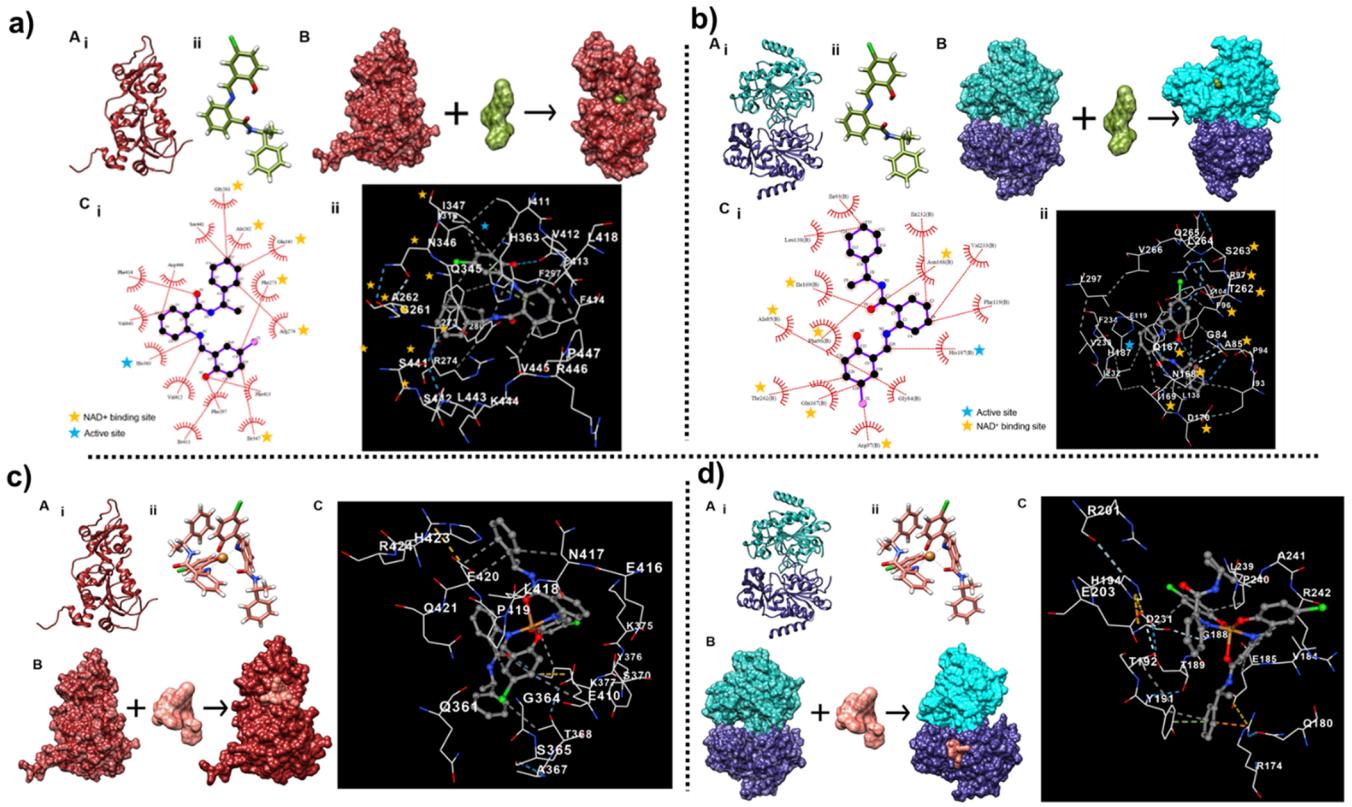

Figure 4. (a) Docking of SIRT1 and HL3. (A) Cartoon representation of the receptor (PDB ID: 4KXQ) (Ai) and stick representation of HL3 (Aii). (B) Surface representation of the receptor, HL3, and docked protein receptor- HL3 complex. (C) Protein−ligand interactions. (Ci) 2D representation of protein- HL3 interactions. Red lines: hydrophobic interactions. (Cii) 3D representation of protein−HL3 interaction in the docked receptor cavity. Dark blue line: strong hydrogen bonds, light blue: weak hydrogen bonds, gray line: hydrophobic interactions. (b) Docking of SIRT2 and HL3. (A) Cartoon representation of the receptor (PDB ID: 4RMJ) (Ai) and stick representation of HL3 (Aii). (B) Surface representation of the receptor, HL3, and docked protein receptor- HL3 complex. (C) Protein−HL3 interactions. (Ci) 2D representation of protein−HL3 interactions. Red lines: hydrophobic interactions. (Cii) 3D representation of protein−ligand interaction in the docked receptor cavity. Dark blue line: strong hydrogen bonds, light blue: weak hydrogen bonds, gray line: hydrophobic interactions. (c) Docking of SIRT1 and $Cu(L3)_2$. (A) Cartoon representation of the receptor (PDB ID: 4KXQ) (Ai) and stick representation of $Cu(L3)_2$ (Aii). (B) Surface representation of the receptor, $Cu(L3)_2$, and docked protein receptor−$Cu(L3)_2$ complex. (C) 3D representation of protein−$Cu(L3)_2$ interaction in the docked receptor cavity. Dark blue line: strong hydrogen bonds, light blue: weak hydrogen bonds, yellow lines: ionic interaction, gray lines: hydrophobic interactions. (d) Docking of SIRT2 and $Cu(L3)_2$. (A) Cartoon representation of the receptor (PDB ID: 4RMJ) (Ai) and stick representation of $Cu(L3)_2$ (Aii). (B) Surface representation of the receptor, $Cu(L3)_2$, and docked protein receptor- $Cu(L3)_2$ complex. (C) 3D representation of protein−$Cu(L3)_2$ interaction in the docked receptor cavity. Dark blue: represents strong hydrogen bonds, light blue: weak hydrogen bonds, olive-green lines: $\pi-\pi$ stacking interactions, orange line: cation−π interaction, yellow lines: ionic interaction, gray lines: hydrophobic interactions.

ion in our biological system could easily transmetallate to show enhanced cytotoxicity. During this process, it becomes interesting to determine whether the inhibitory property of these SIRTi's analogues is retained. Thus, to determine the inhibitory constant, protein−ligand docking of NAD^+-dependent protein deacetylase SIRT1 and SIRT2 with HL3 and $Cu(L3)_2$ was performed using CB-Dock2, incorporating template-independent docking with AutoDock Vina. The crystal structures of SIRT1 (PDB 4KXQ, Uniprot ID: Q96EB6) and SIRT2 (PDB 4RMJ, Uniprot ID: Q8IXJ6) were obtained from the RCSB PDB database.[16−18]

For SIRT1, HL3 was observed to bind within a cavity with a volume of 3554 $Å^3$ (Figure 4a). Docking calculations were performed using a 23 × 32 × 29 Å grid, centered at coordinates (30, −17, 4) Å in the *x*, *y*, and *z* directions, respectively. The resulting docked complex exhibited a Vina score of −9.6 kcal/mol, indicating a favorable binding energy. Analysis of the protein−ligand interactions revealed specific contact residues, including GLY261, ALA262, PHE273, ARG274, TYR280, PHE297, ILE316, GLN345, ASN346, ILE347, HIS363, ILE411, VAL412, PHE413, PHE414, LEU418, SER441, SER442, VAL445, and ARG446. Notably, the ligand interacted with HIS363, a key residue at the active site, as well as GLY261, ALA262, GLN345, PHE273, ARG274, and ILE347 residues involved in NAD+ binding. The K_i value for the HL3 was calculated to be 0.091 μM.

Similarly, $Cu(L2)_2$ was found to bind within another cavity with a volume of 553 $Å^3$, exhibiting a slightly weaker binding affinity with a Vina score of −9.0 kcal/mol compared to the ligand (Figure 4c). The grid dimensions for the metal complex docking were set to 24 × 24 × 24 Å, centered at coordinates (22, −26, −3) Å in the *x*, *y*, and *z* directions, respectively. Analysis of the protein-metal complex interactions revealed contact residues, including GLN361, GLY364, SER365, ALA367, THR368, LYS375, TYR376, LYS377, GLU410, GLU416, ASN417, LEU418, PRO419, GLU420, GLN421, and ARG424. The K_i value calculated for $Cu(L3)_2$ was 0.25 μM, indicating a comparatively lower binding affinity compared to the HL3 ligand.

https://doi.org/10.1021/acsorginorgau.3c00052
ACS Org. Inorg. Au 2024, 4, 319−328

For SIRT2, which is a homomeric dimer in its biologically functional form, HL3 was observed to bind within a cavity located in Chain B of the protein, with a volume of 3609 Å^3 (Figure 4b). Docking calculations were performed using a grid size of 23 × 29 × 23 Å autogrid points, with the grid centered at coordinates (13, −11, −62) Å in the *x*, *y*, and *z* directions, respectively. The resulting docked complex exhibited a Vina score of −9.5 kcal/mol, indicating a favorable binding energy. Analysis of the protein−ligand interactions revealed specific contact residues in Chain B, including GLY84, ALA85, ILE93, PRO94, PHE96, ARG97, TYR104, PHE119, LEU138, GLN167, ASN168, ILE169, ASP170, HIS187, ILE232, VAL233, PHE234, THR262, SER263, LEU264, GLN265, and VAL266. Notably, the ligand interacted with HIS187, a key residue located at the active site, as well as ASN168, ILE169, ALA85, PHE96, THR262, GLN167, and ARG97 residues involved in NAD+ binding. The calculated K_i value for the ligand was 0.108 μM.

In contrast, Cu(L3)$_2$ was found to bind within a cavity in Chain A of the SIRT2 protein, with a volume of 363 Å^3, exhibiting a higher binding affinity compared to the ligand (Figure 4d). Docking calculations for the metal complex were performed using a grid size of 24 × 24 × 24 Å autogrid points, centered at coordinates (21, −24, −28) Å in the *x*, *y*, and *z* directions, respectively. Analysis of the protein−metal complex interactions revealed contact residues, including ARG174, GLN180, VAL184, GLU185, GLY188, THR189, TYR191, THR192, HIS194, ARG201, GLU203, ASP231, LEU239, PRO240, ALA241, and ARG242. The calculated K_i value for the metal complex was 0.06 μM, indicating a comparatively higher binding affinity compared to the ligand.

Overall, the docking simulations provided insights into the specific interactions and binding affinities of the ligand and metal complex with the SIRT1 and SIRT2 proteins. These findings contribute to the understanding of the molecular mechanisms underlying the protein−ligand interactions and have implications for potential therapeutic interventions targeting sirtuin enzymes.

CONCLUSION

Collectively, The research described in this article addresses (i) *de novo* synthesis of Zn(II) complexes of SIRT*i*1/2 analogues and (ii) that undergo transmetalation with Cu(II) ions to generate redox-active copper complexes and generate ROS. (iii) They have proven to amplify the mitochondrial oxidative stress by causing depolarization in the mitochondrial membrane potential ($\Delta\Psi_m$) and depletion in ATP generation. (iv) The mechanistic profile exhibits a ROS mediated paraptosis cell-death pathway, and (v) the computational docking analysis establishes this new class of paraptosis inducer to simultaneously inhibit SIRT1/2 protein. Apoptosis is the primary mechanism by which most anticancer medications induce cell death, there are cases where alternate forms of programmed cell death (PCD) are detected in response to standard therapeutic regimens. Certain anticancer medications exhibit limited effectiveness in eliminating malignant cell lines that possess compromised apoptotic pathways. In such cases, paraptosis emerges as a viable mechanism for inducing cell death, thereby presenting a novel and promising approach for cancer treatment.

This is the first study that demonstrates Zn(II) complexes of SIRT*i*1/2 analogues that undergo transmetalation with redox active Cu(II) ions. Moreover, our study explores the uptake of the paraptosis mediated cell death pathway, which distinguishes it from other SIRT inhibitors that induce cell death through the p53 dependent pathway. The results of our study indicate that the initiation of paraptosis through Zn(II) complexes is linked to the disruption of mitochondrial membrane potential ($\Delta\Psi$m) and the decline of ATP levels. Additionally, we conducted experiments to assess the effectiveness of our complexes in 3D multicellular tumor spheroids (MCTSs), which provide a more accurate means of evaluating the efficacy of drugs compared to 2D monolayer cells. The study's focus on the rational design of a new class of paraptosis inducer as therapeutic agent that aligns perfectly with the new avenues in the field of cancer therapeutics.

EXPERIMENTAL SECTION

Physical Methods and Materials

All of the reagents and solvents were procured from commercial sources (such as TCI Chemicals, Alfa Aesar and Sigma-Aldrich) and used without purification unless otherwise mentioned. The compounds 5-fluoro salicylaldehyde and 5-nitro Salicylaldehyde were synthesized according to previously published literature. The solvents $CDCl_3$ and DMSO-d_6 were employed as solvents for conducting ^{1}H and ^{13}C nuclear magnetic resonance (NMR) experiments on JEOL 400 and 500 MHz spectrometers. The ^{1}H NMR chemical shifts were referenced by using the remaining hydrogen signal of the deuterated solutions. In the context of ^{1}H and ^{13}C NMR spectroscopy, the chemical shift is expressed as dimensionless quantities and calibrated with respect to the TMS as a frequency reference. The ESI-MS data was collected using the Agilent LCMS Q-TOF mass spectrometer. The UV−visible spectra were acquired by utilizing a JASCO V-670 UV−visible absorption spectrophotometer. The Fourier-transform infrared (FT-IR) spectra were obtained by conducting measurements on a PerkinElmer spectrometer within the frequency range of 400−4000 cm^{-1}. These measurements were performed by using potassium bromide (KBr) pellets. The analysis employing high-performance liquid chromatography (HPLC) was performed on an Agilent 1200 apparatus. A flow rate of 1 mL/min was employed, and a gradient was applied, commencing with a mixture consisting of 10% MeCN (acetonitrile) and 90% H_2O (water) and progressively progressing to a composition of 100% MeCN within a time span of 20 min. The investigation was performed by using a diode array detector. The experimental setup involved the utilization of an Agilent Eclipse XDB-C18 column with dimensions of 4.6 × 150 mm and a particle size of 5 μm. The evaluation of purity was conducted by employing an integrated UV chromatogram at a designated wavelength of 220 nm.

The chemicals employed for biological evaluation are required to possess a minimum purity level of 95%.

General Procedure

Synthesis and Characterization of Zn(II) Complexes (ZnL1−ZnL6). *ZnL1*. In a 25 mL round-bottom flask, HL1 (0.1 mmol, 34.4 mg) was dissolved in methanol and triethylamine (3 equiv) was added in that. The reaction mixture was stirred at room temperature. After 5 min, anhydrous $ZnCl_2$ (0.1 mmol, 13.8 mg) was added to the reaction mixture and stirred at room temperature for 4 h. After completion of the reaction, the methanol was removed under reduced pressure. The crude yellow solid product was then redissolved in 3−4 mL of CH_2Cl_2, filtered with cotton, and kept at room temperature to slowly evaporate CH_2Cl_2 to get yellow crystalline product. (Yield: 75%.) ^{1}H NMR (500 MHz, CD_3OD, δ ppm): 8.47 (s, 2H), 7.84−7.61 (m, 4H), 7.41 (d, J = 31.7 Hz, 6H), 7.30−7.15 (m, 12H), 7.13−7.07 (m, 2H), 6.90 (s, 2H), 6.72 (dd, J = 14.7, 7.4 Hz, 2H), 5.06 (d, J = 6.0 Hz, 2H), 1.47 (t, J = 9.6 Hz, 6H). ^{13}C{^{1}H} NMR (101 MHz, CD_3OD, δ ppm): 174.4, 173.8, 172.4, 152.3, 146.7, 140.9, 139.4, 138.0, 133.1, 132.9, 131.0, 129.8, 128.3, 126.3, 126.1, 124.1, 120.5, 54.2, 24.9. ESI-MS+ (m/z): [M + H]+ calcd for [$C_{44}H_{39}N_4O_4Zn$], 751.2263; found, 751.2260.

https://doi.org/10.1021/acsorginorgau.3c00052
ACS Org. Inorg. Au 2024, 4, 319−328

ZnL2. Followed the same procedure as above with ligand HL2 (0.1 mmol, 45.6 mg). The product was yellow in color. (Yield: 68%.) ^{1}H NMR (500 MHz, CD_3OD, δ ppm): 8.42 (s, 2H), 7.75 (d, J = 6.1 Hz, 2H), 7.65 (d, J = 7.5 Hz, 2H), 7.38 (dd, J = 16.7, 7.6 Hz, 10H), 7.26 (dd, J = 13.3, 6.3 Hz, 4H), 7.16 (t, J = 6.6 Hz, 3H), 7.09 (s, 2H), 5.31 (d, J = 5.8 Hz, 2H), 1.53 (d, J = 6.6 Hz, 6H), 1.37 (s, 18H), 1.21 (s, 18H). ^{13}C {^{1}H} NMR (126 MHz, CD_3OD, δ ppm): 170.9, 170.3, 170.0, 149.0, 142.9, 141.0, 135.5, 133.8, 130.3, 129.0, 128.5, 127.1, 126.3, 125.9, 124.4, 121.8, 118.4, 115.6, 50.2, 35.1, 33.5, 30.6, 28.9, 21.0. ESI-MS+ (m/z): [M]+ calcd for [$C_{60}H_{70}N_4O_4Zn$], 974.4789; found, 974.4805.

ZnL3. Followed the same procedure as above with ligand HL3 (0.1 mmol, 37.9 mg). Yellowish crystals were grown in DCM after 24 h at room temperature. (Yield: 73%.) ^{1}H NMR (500 MHz, CD_3OD, δ ppm): 8.43 (s, 2H), 7.91−7.57 (m, 4H), 7.56−6.99 (m, 20H), 6.81 (s, 2H), 5.26 (s, 2H), 1.53 (d, 6H). ^{13}C {^{1}H} NMR (100 MHz, CD_3OD, δ ppm): 168.7, 148.4, 142.9, 134.8, 134.6, 133.9, 129.2, 129.1, 128.4, 128.2, 127.1, 127.0, 125.8, 124.7, 124.3, 122.0, 120.5, 118.9, 50.2, 20.7. ESI-MS+ (m/z): [M]+ calcd for [$C_{44}H_{36}Cl_2N_4O_4Zn$], 818.1405; found, 818.1494.

ZnL4. Followed the same procedure as above with ligand HL4 (0.1 mmol, 43.3 mg). Yellowish crystals were grown in DCM after 24 h at room temperature. (Yield: 70%.) ^{1}H NMR (500 MHz, CD_3OD, δ ppm): 8.42 (s, 2H), 7.77 (s, 2H), 7.67 (s, 2H), 7.53−7.41 (m, 4H), 7.29 (dd, J = 20.9, 14.7 Hz, 14H), 7.19 (t, J = 7.3 Hz, 2H), 6.74 (s, 2H), 5.25 (d, J = 6.9 Hz, 2H), 1.53 (d, J = 6.9 Hz, 6H). ^{13}C {^{1}H} NMR (100 MHz, CD_3OD, δ ppm): 170.5, 169.5, 168.7, 143.0, 137.7, 137.5,133.8, 129.0, 128.4, 128.2, 127.1, 127.0, 125.8, 124.7, 122.0, 121.4, 105.5, 50.2, 20.7. ESI-MS^{+} (m/z): [M + H]$^{+}$ calcd for [$C_{44}H_{37}Br_2N_4O_4Zn$], 906.0473; found, 906.0501.

ZnL5. Followed the same procedure as above with ligand HL5 (0.1 mmol, 36.3 mg). Yellow-orange crystals were grown in DCM after 24 h at room temperature. (Yield: 78%.) ^{1}H NMR (500 MHz, CD_3OD, δ ppm): 8.44 (s, 2H), 7.78 (d, J = 5.9 Hz, 2H), 7.67 (s, 2H), 7.47 (d, J = 7.0 Hz, 2H), 7.41−7.34 (m, 2H), 7.26 (dd, J = 19.7, 12.4 Hz, 2H), 7.20−7.08 (m, 10H), 7.04 (dd, J = 11.1, 5.6 Hz, 4H), 6.85 (s, 2H), 5.19 (d, J = 6.3 Hz, 2H), 1.51 (d, J = 7.1 Hz, 6H). ^{13}C {^{1}H} NMR (126 MHz, CD_3OD, δ ppm): 170.5, 168.7, 154.2, 152.3, 149.0, 148.4, 144.8, 142.9, 141.8, 133.9, 132.7, 129.0, 128.6, 128.4, 127.1, 126.8, 125.8, 124.6, 124.3, 123.7, 123.6, 123.0, 122.8, 122.5, 122.0, 119.6, 119.5, 119.3, 119.0, 118.90, 50.2, 20.8. ESI-MS+ (m/z): [M + H]+ calcd for [$C_{44}H_{37}F_2N_4O_4Zn$], 787.2074; found, 787.2064.

ZnL6. Followed the same procedure as above with ligand HL6 (0.1 mmol, 38.9 mg). Yellowish crystals were grown in DCM after 24 h at room temperature on the wall of the vial. (Yield: 61%.) ^{1}H NMR (400 MHz, CD_3OD, δ ppm): 8.56 (s, 2H), 8.41 (d, J = 2.9 Hz, 2H), 8.04 (dd, J = 9.5, 3.0 Hz, 2H), 7.84−7.78 (m, 2H), 7.69 (t, J = 7.6 Hz, 2H), 7.49 (t, J = 7.6 Hz, 2H), 7.41 (d, J = 7.9 Hz, 2H), 7.36 (d, J = 7.4 Hz, 4H), 7.26 (t, J = 7.6 Hz, 4H), 7.17 (d, J = 7.3 Hz, 2H), 6.74 (d, J = 9.5 Hz, 2H), 5.25 (d, J = 7.0 Hz, 2H), 1.53 (d, J = 7.0 Hz, 6H). ^{13}C {^{1}H} NMR (100 MHz, CD_3OD, δ ppm): 180.3, 174.5, 172.7, 172.6, 151.9, 147.0, 139.6, 138.3, 138.0, 133.2, 132.4, 131.5, 131.1, 129.8, 128.4, 127.4, 126.3, 122.7, 54.5, 25.2. ESI-MS+(m/z): [M + H]+ calcd for [$C_{44}H_{37}N_6O_4Zn$], 841.1964; found, 841.1961.

■ ASSOCIATED CONTENT

Data Availability Statement

The data underlying this study are available in the published article and its Supporting Information.

Supporting Information

The Supporting Information is available free of charge at https://pubs.acs.org/doi/10.1021/acsorginorgau.3c00052.

Synthetic methods, characterization of the ligands and the complexes (^{1}H and ^{13}C NMR, IR, UV−vis, HPLC, single crystal X-ray diffraction, and protocols for biological assays (PDF)

Accession Codes

CCDC 2294883−2294885 and 2295142 contain the supplementary crystallographic data for this paper. These data can be obtained free of charge via www.ccdc.cam.ac.uk/data_request/cif, or by emailing data_request@ccdc.cam.ac.uk, or by contacting The Cambridge Crystallographic Data Centre, 12 Union Road, Cambridge CB2 1EZ, UK; fax: +44 1223 336033.

■ AUTHOR INFORMATION

Corresponding Author

Ritika Gautam Singh − *Department of Chemistry, Indian Institute of Technology Kanpur, Kanpur 208016, India;* orcid.org/0000-0001-5826-0719; Email: rgautam@iitk.ac.in

Authors

Ashwini Kumar − *Department of Chemistry, Indian Institute of Technology Kanpur, Kanpur 208016, India*

Ayushi Chaudhary − *Department of Chemistry, Indian Institute of Technology Kanpur, Kanpur 208016, India*

Himanshu Sonker − *Department of Chemistry, Indian Institute of Technology Kanpur, Kanpur 208016, India*

Seemadri Subhadarshini − *Molecular Biophysics Unit, Indian Institute of Science, Bangalore 560012, India*

Mohit K. Jolly − *Department of Bioengineering, Indian Institute of Science, Bangalore 560012, India*

Complete contact information is available at: https://pubs.acs.org/10.1021/acsorginorgau.3c00052

Author Contributions

The manuscript was written through the contributions of all authors. All authors have given approval to the final version of the manuscript. A.K. executed the synthesis and characterization, A.K. and A.C. worked on cell-based assays, H.S. did the X-ray analysis, S.S. and M.K.J. performed docking and computational analysis. CRediT: **Ashwini Kumar** conceptualization, data curation, formal analysis, project administration; **Ayushi Chaudhary** conceptualization, data curation, methodology; **Himanshu Sonker** formal analysis; **Seemadri Subhadarshini** data curation, formal analysis; **Mohit Kumar Jolly** resources, software, supervision, validation, visualization.

Funding

This work was supported by Ritika Gautam's DST SERB Start-up Research Grant (Grant 2021435) and INSPIRE Faculty Research Grant (Grant 2019295), and Ashwini's Prime Minister Research Grant (PMRF-ID: 2300572). Mohit Kumar Jolly is supported by the Ramanujan Fellowship awarded by SERB (Science and Engineering Research Board), Department of Science and Technology (DST), Government of India (SB/S2/RJN-049/2018). Seemadri is supported by the Prime Ministers' Research Fellowship (PMRF ID- 200119)

Notes

The authors declare no competing financial interest.

■ ACKNOWLEDGMENTS

We would also like to extend our gratitude to Dr. Shweta Khanna, for initial help in cell-culture practices and Mr. Ramesh Singh, for collecting single-crystal X-ray diffraction data. We are grateful to Prof. S. Ganesh laboratory, BSBE department at IITK for providing us access to plate reader

(SpectraMax M5) (concerned person Ms. Monica Shukla) and Prof. Sandeep Verma's Lab (Chemistry Department, IITK) for providing us access to their HPLC instrument.

REFERENCES

(1) Grozinger, C. M.; Chao, E. D.; Blackwell, H. E.; Moazed, D.; Schreiber, S. L. Identification of a Class of Small Molecule Inhibitors of the Sirtuin Family of NAD-dependent Deacetylases by Phenotypic Screening. *J. Biol. Chem.* **2001**, *276*, 38837−38843.
(2) Gautam, R.; Akam, E. A.; Astashkin, A. V.; Loughrey, J. J.; Tomat, E. Sirtuin inhibitor sirtinol is an intracellular iron chelator. *Chem. Commun.* **2015**, *51*, 5104−5107.
(3) Ota, H.; Tokunaga, E.; Chang, K.; Hikasa, M.; Iijima, K.; Eto, M.; et al. Sirt1 inhibitor, Sirtinol, induces senescence-like growth arrest with attenuated Ras-MAPK signaling in human cancer cells. *Oncogene* **2006**, *25*, 176−185.
(4) Akam, E. A.; Gautam, R.; Tomat, E. Metal binding effects of sirtuin inhibitor sirtinol. *Supramol. Chem.* **2016**, *28*, 108−116.
(5) Fekri, R.; Salehi, M.; Asadi, A.; Kubicki, M. Synthesis, Characterization, Anticancer and Antibacterial Evaluation of Schiff Base Ligands Derived from Hydrazone and Their Transition Metal Complexes. *Inorg. Chim. Acta* **2019**, *484*, 245−254.
(6) French, F. A.; Blanz, E. J., Jr. The carcinostatic activity of thiosemicarbazones of formyl heteroaromatic compounds. 3. Primary correlation. *J. Med. Chem.* **1966**, *9*, 585−589.
(7) Kumar, A.; Chaudhary, A.; Agrahari, B.; Chaudhary, K.; Kumar, P.; Singh, R. G. Concurrent Cu(II)-initiated Fenton-like reaction and glutathione depletion to escalate chemodynamic therapy. *Chem. Commun.* **2023**, *59*, 14305−14308.
(8) van Rijt, S. H.; Sadler, P. J. Current applications and future potential for bioinorganic chemistry in the development of anticancer drugs. *Drug Discovery Today* **2009**, *14*, 1089−1097.
(9) Stacy, A. E.; Palanimuthu, D.; Bernhardt, P. V.; Kalinowski, D. S.; Jansson, P. J.; Richardson, D. R. Zinc(II)-Thiosemicarbazone Complexes Are Localized to the Lysosomal Compartment Where They Transmetallate with Copper Ions to Induce Cytotoxicity. *J. Med. Chem.* **2016**, *59*, 4965−84.
(10) Yumnam, S.; et al. Mitochondrial dysfunction and Ca2+ overload contribute to hesperidin-induced paraptosis in hepatoblastoma cells, HepG2. *J. Cell. Physiol.* **2016**, *231*, 1261−1268.
(11) Wang, Y.; Wen, X.; Zhang, N.; Wang, L.; Hao, D.; Jiang, X.; He, G. Small-molecule compounds target paraptosis to improve cancer therapy. *Biomed. Pharmacother.* **2019**, *118*, 109203−109214.
(12) Crouch, S. P.; Kozlowski, R.; Slater, K. J.; Fletcher, J. The use of ATP bioluminescence as a measure of cell proliferation and cytotoxicity. *J. Immunol. Method.* **1993**, *160*, 81−88.
(13) Dharmasivam, M.; Kaya, B.; Wijesinghe, T. P.; Richardson, V.; Harmer, J. R.; Gonzalvez, M. A.; Lewis, W.; Azad, M. G.; Bernhardt, P. V.; Richardson, D. R. Differential transmetallation of complexes of the anti-cancer thiosemicarbazone, Dp4e4mT: effects on anti-proliferative efficacy, redox activity, oxy-myoglobin and oxy-hemoglobin oxidation. *Chem. Sci.* **2024**, *15*, 974−990.
(14) Kalyanaraman, B.; Darley-Usmar, V.; Davies, K. J. A.; Dennery, P. A.; Forman, H. J.; Grisham, M. B.; Mann, G. E.; Moore, K.; Roberts, L. J.; Ischiropoulos, H. Measuring reactive oxygen and nitrogen species with fluorescent probes: challenges and limitations. *Free Radic. Biol. Med.* **2012**, *52*, 1−6.
(15) Karlsson, M.; Kurz, T.; Brunk, U. T.; Nilsson, S. E.; Frennesson, C. I. What does the commonly used DCF test for oxidative stress really show? *Biochem. J.* **2010**, *428*, 183−90.
(16) Liu, Y.; Yang, X.; Gan, J.; Chen, S.; Xiao, Z. X.; Cao, Y. CB improved protein−ligand blind docking by integrating cavity detection, docking and homologous template fitting. *Nucleic Acids Res.* **2022**, *50*, W159−W164.
(17) Laskowski, R. A.; Swindells, M. B. LigPlot+: multiple ligand-protein interaction diagrams for drug discovery. *J. Chem. Inf. Model.* **2011**, *51*, 2778−86.
(18) Pettersen, E. F.; Goddard, T. D.; Huang, C. C.; Couch, G. S.; Greenblatt, D. M.; Meng, E. C.; et al. UCSF Chimera–a visualization system for exploratory research and analysis. *J. Comput. Chem.* **2004**, *25*, 1605−12.

https://doi.org/10.1021/acsorginorgau.3c00052
ACS Org. Inorg. Au 2024, 4, 319−328